Snakes with Ellipse-Reproducing Property

Ricard Delgado-Gonzalo, Philippe Thévenaz, Chandra Sekhar Seelamantula, and Michael Unser

***Abstract*—We present a new class of continuously defined parametric snakes using a special kind of exponential splines as basis functions. We have enforced our bases to have the shortest-possible support subject to some design constraints to maximize efficiency. While the resulting snakes are versatile enough to provide a good approximation of any closed curve in the plane, their most important feature is the fact that they admit ellipses within their span. Thus, they can perfectly generate circular and elliptical shapes. These features are appropriate to delineate cross sections of cylindrical-like conduits and to outline blob-like objects. We address the implementation details and illustrate the capabilities of our snake with synthetic and real data.**

***Index Terms*—Exponential B-spline, parametric snake, active contour, parameterization, segmentation.**

Fig. 1. Approximation capabilities of the proposed parametric snake. The thin solid line corresponds to an elliptical fit. The dashed thick line corresponds to a generalized shape.

I. Introduction

ACTIVE contours, and snakes in particular, are effective tools for image segmentation. Within an image, an active contour is a curve that evolves from an initial position, which is usually specified by a user, toward the boundary of an object. The evolution of the curve is formulated as a minimization problem. The associated cost function is called *snake energy*. Snakes have become popular because it is possible for the user to interact with them, not only when specifying its initial position, but also during the segmentation process.

Research in this area has been fruitful and has resulted in many snake variants [1], [2]. They differ in the type of curve representation and in the choice of the energy term [3]. Snakes can be broadly categorized in terms of curve representation as

- point-snakes, where the curve is described in a discrete fashion by a set of points [4], [5], [6];
- parametric snakes, where the curve is described continuously by some coefficients using basis functions [7], [8], [9], [10], [11];
- implicit snakes, where the representation of the curve is implicit and described as the level-set of a surface [12], [13], [14], [15].

Point-snakes can be viewed as a special case of parametric snakes where a large number of coefficients is used [10]. Parametric snakes require fewer parameters and result in faster optimization. It can be shown that the computation complexity of the snake energy, and, therefore, the speed of the optimization algorithms is related to the size of the support of the basis functions [3]. It is therefore critical to minimize this support while designing parametric snakes. The curve of parametric snakes is represented explicitly, so that it is easy to introduce smoothness and shape constraints [7]. It is also straightforward to accommodate user interaction. This is often achieved by allowing the user to specify some anchor points the curve should go through [4]. The downsize of the method is that the topology of the curve is imposed by the parameterization. This makes parametric snakes less suitable for handling topological changes, although solutions have been proposed for specific cases [16], [17].

Implicit approaches offer great flexibility as far as the curve topology is considered [18]. However, they tend to be computationally more expensive since they evolve a 2-D surface rather than a 1-D curve.

In this paper, we design fast parametric snakes capable of perfectly outlining elliptic objects and yet versatile enough to provide a close approximation of any closed curve in the plane. We illustrate in Figure 1 how our snake can adopt the shape of a perfect ellipse (*i.e.* reproduces the ellipse) as well as more refined shapes. Segmenting circles and ellipses in images is a problem that arises in many fields, for example biomedical engineering [19], [20], [21], [22] or computer graphics [23], [24]. In medical imaging in particular, it is usually necessary to segment arteries and veins within tomographic slices [25]. Because those objects are physiological tubes, their section show up as ellipses in the image. Ellipse-like objects are also present at microscopic scales. For instance, cell nuclei are known to be nearly circular [26] and water drops are similarly spherical thanks to surface-tension forces [27]. However, these elements deform and become elliptical when they are subject to stress forces.

R. Delgado-Gonzalo, P. Thévenaz, and M. Unser are with the Biomedical Imaging Group, École polytechnique fédérale de Lausanne (EPFL), Switzerland. C.S. Seelamantula is with the Department of Electrical Engineering, Indian Institute of Science (IISc), Bangalore, India.

This work was funded by the Swiss SystemsX.ch initiative under Grant 2008/005 and the Swiss National Science Foundation under Grant 200020-121763.

In order to efficiently segment elliptical objects, a parametric snake named the Ovuscule was proposed in [28]. It is a minimalistic elliptical snake defined by three control points. Its main drawback was that it was unable to represent shapes different from circles and ellipses. Our goal here is to create a more versatile parametric snake whose basis functions are short, perfectly reproduce ellipses, and have good approximation properties. Our main contribution in this paper is to fulfill this goal by selecting a special kind of exponential B-splines. We are actually able to prove that our basis functions are the ones with the shortest support among all admissible functions. Since the computational cost of spline snakes is determined in part by the size of the support of the basis function, our use of the shortest possible support favors optimal performance.

The paper is organized as follows: In Section II we review the general parametric snake model and formalize our design constraints. Our main contribution is described in Section III, where we build an explicit expression for the underlying basis functions that fulfill our requirements, and we analyze in detail its reproduction and approximation properties. Implementation details such as energy functionals and discretization issues are addressed in Section IV. Finally, we perform report evaluations in Section V.

II. Parametric Snakes

A. Parametric Representation of Closed Curves

A curve $\mathbf{r}(t)$ on the plane can be described by a pair of Cartesian coordinate functions $x_1(t)$ and $x_2(t)$, where $t \in \mathbb{R}$ is a continuous parameter. The one-dimensional functions x_1 and x_2 are efficiently parameterized by linear combinations of suitable basis functions. Among all possible bases, we focus on those derived from a compactly supported generator φ and its integer shifts $\{\varphi(\cdot - k)\}_{k\in\mathbb{Z}}$. This allows us to take advantage of the availability of fast and stable interpolation algorithms [29].

We are interested in close curves specified by an M-periodic sequence of control points $\{\mathbf{c}[k]\}_{k\in\mathbb{Z}}$, with $\mathbf{c}[k] = \mathbf{c}[k+M]$. The parametric representation of the curve is then given by the vectorial equation

$$\mathbf{r}(t) = \sum_{k=-\infty}^{\infty} \mathbf{c}[k]\, \varphi(M\, t - k). \tag{1}$$

The number of control points M determines the degrees of freedom in the model (1). Small numbers lead to constrained shapes, and large numbers lead to additional flexibility and more general shapes.

Since the curve $\mathbf{r}$ is closed, each coordinate function is periodic, and the period is common for both. For simplicity, in (1) we normalized this period to be unity. Under these conditions, we can reduce the infinite summation in (1) to a finite one involving periodized basis functions as

$$\begin{aligned}\mathbf{r}(t) &= \sum_{k=0}^{M-1} \sum_{n=-\infty}^{\infty} \mathbf{c}[M\, n + k]\, \varphi(M\ (t-n) - k) \\ &= \sum_{k=0}^{M-1} \mathbf{c}[k] \underbrace{\sum_{n=-\infty}^{\infty} \varphi(M\ (t-n) - k)}_{\varphi_M(M\,t-k)}, \end{aligned} \tag{2}$$

where φ_M is the M-periodization of the basis function φ.

This kind of curve parameterization is general. Using this model, we can approximate any closed curve as accurately as desired by using a higher number of vector coefficients $M_2 > M$, provided that φ satisfies some mild conditions [30].

B. Desirable Properties for the Basis Functions

We now enumerate the conditions that our parametric snake model should satisfy and introduce the corresponding mathematical formalism.

1) *Unique and Stable Representation*. We want our parametric curve to be defined in terms of the coefficients in such a way that unicity of representation is satisfied. Furthermore, for computational purposes, we ask the interpolation procedure to be numerically stable.
A generating function φ is said to satisfy the Riesz basis condition if and only if there exist two constants $0 < A \leq B < \infty$ such that

$$A\ \|\mathbf{c}\|_{\ell_2} \leq \sqrt{M} \left\| \sum_{k=-\infty}^{\infty} \mathbf{c}[k]\, \varphi(M\ \cdot - k) \right\|_{L_2} \leq B\ \|\mathbf{c}\|_{\ell_2} \tag{3}$$

for all $\mathbf{c} \in \ell_2$. A direct consequence of the lower inequality is that the condition $\sum_{k=-\infty}^{\infty} \mathbf{c}[k]\, \varphi(M\,t - k) = 0$ for all $t \in \mathbb{R}$ implies that $\mathbf{c}[k] = 0$ for all $k \in \mathbb{Z}$. Thus, the basis functions are linearly independent and every function is uniquely specified by its coefficients. The upper inequality ensures the stability of the interpolation process [29].
It has been shown in [31] that, due to the integer-shift-invariant structure of the representation, the Riesz condition has the following equivalent expression in the Fourier domain:

$$A \leq \sum_{k=-\infty}^{\infty} |\hat{\varphi}(\cdot + 2\,\pi\, k)|^2 \leq B,$$

where $\hat{\varphi}(\omega) = \int_{\mathbb{R}} \varphi(x)\, \mathrm{e}^{-\mathrm{j}\,\omega\, x} \mathrm{d}x$ denotes the Fourier transform of φ. Once expressed in the Fourier domain, the Riesz condition provides a practical way to verify if a given generating function φ satisfies (3).

2) *Affine Invariance*. Since we are interested in outlining shapes irrespective of their position and orientation, we would like our model to be invariant to affine transformations, which we formalize as

$$\mathbf{A}\, \mathbf{r}(t) + \mathbf{b} = \sum_{k=-\infty}^{\infty} (\mathbf{A}\, \mathbf{c}[k] + \mathbf{b})\ \varphi(M\, t - k), \tag{4}$$

where $\mathbf{A}$ is a (2×2) matrix and $\mathbf{b}$ is a two-dimensional vector. From (4), it is easy to show that affine invariance is ensured if and only if

$$\forall t \in \mathbb{R} : \sum_{k=-\infty}^{\infty} \varphi(M\, t - k) = 1. \tag{5}$$

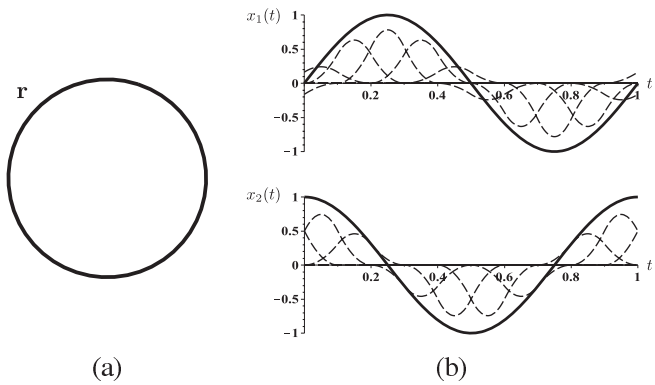

Fig. 2. Parametric representation of the unit circle (a) and its coordinate functions (b) with exponential B-splines and $M = 10$. The dashed lines in (b) indicate the corresponding basis functions.

In the literature, this constraint is often named the *partition-of-unity* condition [29].

3) *Well-Defined Curvature*. The curvature of a parametric curve at a point $(x_1(t), x_2(t))$ is given by

$$\kappa(x_1, x_2) = \frac{\dot{x}_1\,\ddot{x}_2 - \ddot{x}_1\,\dot{x}_2}{(\dot{x}_1^2 + \dot{x}_2^2)^{3/2}},$$

where the dot denotes the derivative with respect to t. We would like to be able to compute κ for every point on the snake. To do so, each coordinate function (or, equivalently, the basis φ) must be at least twice differentiable and its second derivative must be bounded.

III. Reproduction of Ellipses

Since every ellipse can be obtained by applying an affine transformation to the unit circle, we focus on the reproduction of this simpler shape. This simplification is allowed whenever the affine-invariance requirement stated in Section II-B is satisfied.

A parametric snake defined by M vectorial coefficients and by a generating function φ is said to reproduce the unit circle if there exist two M-periodic sequences $\{c_1[k]\}_{k\in\mathbb{Z}}$ and $\{c_2[k]\}_{k\in\mathbb{Z}}$ such that

$$\cos(2\,\pi\,t) = \sum_{k=-\infty}^{\infty} c_1[k]\,\varphi(M\,t - k) \tag{6}$$

$$\sin(2\,\pi\,t) = \sum_{k=-\infty}^{\infty} c_2[k]\,\varphi(M\,t - k). \tag{7}$$

That is, we need to be able to reproduce sinusoids of unit period for each component of the parametric snake, as illustrated in Figure 2. Note that, when (6) and (7) hold, it is possible to represent any sinusoid of unit period for an arbitrary initial phase using linear combinations of the two sequences of coefficients.

A. Minimum-Support Ellipse-Reproducing Basis

We now present and prove our main result. We provide an explicit expression for the minimum-support basis functions that reproduce sinusoids.

Theorem 1: The centered generating function with minimal support that satisfies all conditions in Section II-B and reproduces sinusoids of unit period with M coefficients is

$$\varphi(t) = \begin{cases} \frac{\cos\frac{2\,\pi\,|t|}{M}\,\cos\frac{\pi}{M} - \cos\frac{2\,\pi}{M}}{1-\cos\frac{2\,\pi}{M}} & 0 \le |t| < \frac{1}{2} \\ \frac{1-\cos\frac{2\,\pi\,(3/2-|t|)}{M}}{2\left(1-\cos\frac{2\,\pi}{M}\right)} & \frac{1}{2} \le |t| < \frac{3}{2} \\ 0 & \frac{3}{2} \le |t|\,. \end{cases} \tag{8}$$

In order to prove Theorem 1, we refer to the Distributional Decomposition Theorem detailed in [32]. This Decomposition Theorem provides a complete characterization of the family of basis functions with minimum-support that reproduce exponential polynomials. It states that every minimum support function φ that reproduces exponentials $\mathrm{e}^{\alpha_n\,t}$, for all $n \in [0 \ldots N-1]$ with $\alpha_i - \alpha_j \notin 2\,\pi\,\mathrm{j}\,\mathbb{Z}$, can be written as

$$\varphi(t) = \sum_{n=0}^{N-1} \lambda_n\,\frac{\mathrm{d}^n}{\mathrm{d}t^n}\beta_{\boldsymbol{\alpha}}(t-a), \tag{9}$$

where a is an arbitrary shift parameter that corresponds to the lower extremity of the support of φ, and where $\beta_{\boldsymbol{\alpha}}$ is the appropriate exponential B-spline

$$\hat{\beta}_{\boldsymbol{\alpha}}(\omega) = \prod_{n=1}^{N} \frac{1 - \mathrm{e}^{\alpha_n - \mathrm{j}\,\omega}}{\mathrm{j}\,\omega - \alpha_n}. \tag{10}$$

Note that exponential B-splines are entirely specified by the collection $\boldsymbol{\alpha} = (\alpha_1, \ldots, \alpha_N)$. The ordering of the poles α_n is irrelevant. A complete survey of the properties of exponential B-splines can be found in [33].

We finally have the mathematical tools to justify our choice for the generating function in (8).

Proof: Using (9), we see that φ needs to be constructed from combinations of exponential B-splines with parameters $\boldsymbol{\alpha} = (0, \mathrm{j}\,\frac{2\pi}{M}, -\mathrm{j}\,\frac{2\pi}{M})$ and $N = 3$. Therefore, we have

$$\varphi(t) = \sum_{n=0}^{2} \lambda_n\,\frac{\mathrm{d}^n}{\mathrm{d}t^n}\,\beta_{\boldsymbol{\alpha}}(t-a). \tag{11}$$

This ensures that φ is the shortest generating function that reproduces constants and all sinusoids of unit period with M coefficients. The constant-reproduction property is a direct consequence of using $\alpha_0 = 0$, and the sinusoids-reproduction property can be proved by using $\alpha_1 = \mathrm{j}\,\frac{2\pi}{M}$, $\alpha_2 = -\mathrm{j}\,\frac{2\pi}{M}$, and Euler's identity.

Using properties of exponential B-splines, we know that $\beta_{\boldsymbol{\alpha}}$ is twice differentiable. Moreover, the second derivative is bounded but may be discontinuous. Therefore, λ_1 and λ_2 in (11) must vanish to ensure that the curvature of the snake is well-defined. Since φ reproduces constants, λ_0 can be computed by imposing the partition-of-unity condition. From (5), we have that

$$\lambda_0 = \frac{\left(\frac{2\pi}{M}\right)^2}{2\,\left(1 - \cos\frac{2\pi}{M}\right)}.$$

Exponential B-splines parameterized by $\boldsymbol{\alpha}$ form a Riesz basis if and only if $\alpha_{m_1} - \alpha_{m_2} \notin 2\,\pi\,\mathrm{j}\,\mathbb{Z}$ for all pairs such that $m_1 \neq m_2$. In our case, it is important to realize that this condition is satisfied if and only if $M \geq 3$. In other words, at

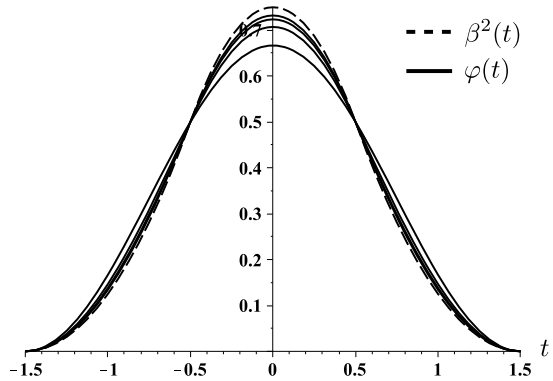

Fig. 3. Plot of a quadratic B-spline β^2 and the resulting generating functions given in (8) for $M = 3$, 4, 5, and 6. The function with the lowest peak at $t = 0$ corresponds to $M = 3$, and as M increases, the height of the central peak increases as well.

least three control points are needed to define our parametric snake.

Finally, a closed form for φ is obtained by applying the inverse Fourier transform to (11), which yields

$$\hat{\varphi}(\omega) = \lambda_0 \, \mathrm{e}^{\mathrm{j}\,\frac{3\,\omega}{2}} \, \frac{1 - \mathrm{e}^{-\mathrm{j}\,\omega}}{\mathrm{j}\,\omega} \, \frac{1 - \mathrm{e}^{\mathrm{j}\,\frac{2\,\pi}{M} - \mathrm{j}\,\omega}}{\mathrm{j}\,\omega - \mathrm{j}\,\frac{2\,\pi}{M}} \, \frac{1 - \mathrm{e}^{-\mathrm{j}\,\frac{2\,\pi}{M} - \mathrm{j}\,\omega}}{\mathrm{j}\,\omega + \mathrm{j}\,\frac{2\,\pi}{M}},$$

where we have set $a = -\frac{3}{2}$ in order to ensure that the basis function is centered. ■

We show in Figure 3 some members of this family of functions for several values of M. We observe that they share with the quadratic B-spline a finite support of length $W = 3$. Likewise, they are one-time continuously differentiable and have a similar bump-like appearance.

B. Approximation Properties of φ

Not only are we interested in reproducing ellipses, but we would like our snake to be able to approximate any other shape $\mathbf{s}$. This is achieved by increasing the number of degrees of freedom afforded by the number M of nodes. In the Fourier domain, it is easy to see that φ converges to a quadratic B-spline as M increases. Therefore, we expect similar approximation properties for large values of M.

While φ leads to integer-shift invariance, the space spanned by the generating function φ is not shift-invariant in general. Hence, the approximation error using M vector coefficients is dependent upon a shift in the continuous parameter t of the 1-periodic function $\mathbf{s}$. The minimum-mean-square approximation error for a shifted function is given by

$$\begin{aligned} \gamma(\tau, M) &= \int_0^1 \|\mathbf{s}(t-\tau) - \mathbf{r}(t)\|^2 \, \mathrm{d}t \\ &= \|\mathbf{s}(\cdot - \tau) - \mathbf{r}(\cdot)\|^2_{L_2([0,1])}, \end{aligned}$$

where $\mathbf{r}$ is the best approximation within the span $\{\varphi(M \cdot - k)\}_{k\in\mathbb{Z}}$. Since τ is usually unknown, we measure the error averaged over all possible shifts as

$$\eta(M) = \left(\int_0^1 \gamma(\tau, M) \, \mathrm{d}\tau \right)^{\frac{1}{2}}. \tag{12}$$

We give in Section III-C the decay of η as $M \to \infty$, following the method described in [30]. As expected, we find that the best averaged-quadratic-mean error decays as $1/M^3$ when the number of vector coefficients M increases—the same rate as the quadratic B-spline [34].

C. Approximation Order of φ

In this section, we introduce the necessary formalism to compute the order of the approximation error associated to the best-possible approximation of a periodic vector function $\mathbf{s}$ within the span of the basis $\{\varphi(M \cdot - k)\}_{k\in\mathbb{Z}}$, where φ is given by (8).

As explained in Section III-B about the approximation properties of φ, the space spanned by the generating function φ is not shift-invariant in general. Hence, as a metric of dissimilarity between shapes, we use the averaged minimum-mean-square approximation error η.

Using the main result of [30], we obtain the asymptotic behavior of η as

$$\begin{aligned} \eta^2(M) &= C_1^2(M) \, \|\dot{\mathbf{s}}\|^2_{L_2([0,1])} \, M^{-2} \\ &\quad + C_2^2(M) \, \|\ddot{\mathbf{s}}\|^2_{L_2([0,1])} \, M^{-4} + \mathcal{O}\left(M^{-6}\right), \end{aligned}$$

where $C_L = \frac{1}{L!} \sqrt{\left(\sum_{k\neq 0} \left| \hat{\varphi}^{(L)}(2\,\pi\,k) \right|^2 \right)}$ and $\hat{\varphi}^{(L)}$ is the L-th derivative of the Fourier transform of φ. Following lengthy calculations, we get (13) and (14), where we defined $M_0 = \pi \cot \frac{\pi}{M}$. It can be shown that $C_1(M) = \mathcal{O}(M^{-2})$ and $C_2(M) = \mathcal{O}(M^{-2})$. Since the curve $\mathbf{s}$ does not depend on M, we can also write that

$$\eta(M) = \left(\mathcal{O}\left(M^{-6}\right) \right)^{\frac{1}{2}} = \mathcal{O}\left(M^{-3}\right),$$

which shows that the averaged quadratic mean error decays as M^{-3}.

D. Best Constant and Ellipse Fitting

Since our snakes have the capability of perfectly reproducing ellipses, it is natural to ask which is the best ellipse that approximates the parametric curve $\mathbf{r}$ defined by the M-periodic sequence $\{\mathbf{c}[k]\}_{k\in\mathbb{Z}}$. In other words, we are interested in finding the ellipse $\mathbf{r}_\mathrm{e}$ that minimizes

$$\|\mathbf{r} - \mathbf{r}_\mathrm{e}\|^2_{L_2([0,1])} = \int_0^1 \|\mathbf{r}(t) - \mathbf{r}_\mathrm{e}(t)\|^2 \, \mathrm{d}t.$$

Since $\mathbf{r}$ is continuous and 1-periodic, we can expand it in a Fourier series as

$$\mathbf{r}(t) = \sum_{n=-\infty}^{\infty} \mathbf{R}[n] \, \mathrm{e}^{\mathrm{j}\,2\,\pi\,n\,t}. \tag{15}$$

The Fourier-series vector coefficients $\mathbf{R}$ in (15) are given by

$$\begin{aligned} \mathbf{R}[n] &= \int_0^1 \mathbf{r}(t) \, \mathrm{e}^{-\mathrm{j}\,2\,\pi\,n\,t} \, \mathrm{d}t \\ &= \frac{1}{M} \, \hat{\varphi}\left(\frac{2\,\pi\,n}{M}\right) \sum_{k=0}^{M-1} \mathbf{c}[k] \, \mathrm{e}^{-\mathrm{j}\,\frac{2\,\pi}{M}\,n\,k}, \end{aligned} \tag{16}$$

where the parametric expression of $\mathbf{r}$ has been used in the second equality.

$$C_1(M) = \frac{1}{12\,\pi}\sqrt{18\,(M_0 - M)\,(M_0 + 4\,M) + 30\,\pi^2} \tag{13}$$

$$C_2(M) = \frac{1}{120\,\pi^2}\sqrt{225\,(2\,M_0^4 - 7\,M^2\,M_0^2 - 15\,M^3\,M_0 + 20\,M^4) + 75\,(8\,M_0^2 - 29\,M^2)\,\pi^2 + 170\,\pi^4} \tag{14}$$

From the classical theory of harmonic analysis, we know that the best ellipse approximation (component-wise sinusoids) of $\mathbf{r}$, in the $L_2([0,1])$ sense, is the first-order truncation of the series (15), where only the terms $n=-1$, $n=0$, and $n=1$ are kept. Therefore, we have that

$$\begin{aligned}\mathbf{r}_{\mathrm{e}}(t) &= \mathbf{R}[0] + (\mathbf{R}[1] + \mathbf{R}[-1])\,\cos(2\,\pi\,t) \\ &\quad + \mathrm{j}\,(\mathbf{R}[1] - \mathbf{R}[-1])\,\sin(2\,\pi\,t)\,,\end{aligned} \tag{17}$$

where $\mathbf{R}[0]$ is the center of gravity of the snake. The Fourier coefficients in (17) can easily be obtained from (16) as

$$\begin{aligned}\mathbf{R}[0] &= \frac{1}{M}\sum_{k=0}^{M-1}\mathbf{c}[k] \\ \mathbf{R}[1] + \mathbf{R}[-1] &= \sum_{k=0}^{M-1} h_{\mathrm{c}}[k]\,\mathbf{c}[k] \\ \mathrm{j}\,(\mathbf{R}[1] - \mathbf{R}[-1]) &= \sum_{k=0}^{M-1} h_{\mathrm{s}}[k]\,\mathbf{c}[k],\end{aligned}$$

where

$$\begin{aligned}h_{\mathrm{c}}[k] &= \frac{2}{M}\,\cos\frac{\pi}{M}\,\cos\frac{2\,\pi\,k}{M} \\ h_{\mathrm{s}}[k] &= \frac{2}{M}\,\cos\frac{\pi}{M}\,\sin\frac{2\,\pi\,k}{M}.\end{aligned}$$

Since all sinusoids of unit period can be reproduced by the generating function φ and the appropriate M-periodic sequence of coefficients $\mathbf{c}$, the curve $\mathbf{r}_{\mathrm{e}}$ belongs to the span of φ. For the sake of completeness, we provide in the next section an explicit expansion of sinusoids in terms of φ.

E. Expansion of Sinusoids with φ

Here, we explicitly find the sequence of M vector coefficients that reproduce sinusoids of unit period using the generating function φ given in (8). We start by recalling the exponential-reproducing property of the exponential B-splines as

$$\mathrm{e}^{\alpha\,t} = \sum_{k=-\infty}^{\infty} \mathrm{e}^{\alpha\,k}\,\beta_{(\alpha)}(t-k). \tag{18}$$

Setting $\alpha = \mathrm{j}\,\frac{2\,\pi}{M}$, we see that $\beta_{(\mathrm{j}\,\frac{2\,\pi}{M})}$ reproduces the complex exponential $\mathrm{e}^{\mathrm{j}\,\frac{2\,\pi}{M}\,t}$, which is M-periodic. If we now convolve both sides of (18) with $\beta_{(0,-\mathrm{j}\,\frac{2\,\pi}{M})}$, we get that

$$\begin{aligned}&\left(\beta_{(0,-\mathrm{j}\,\frac{2\,\pi}{M})} * \mathrm{e}^{\mathrm{j}\,\frac{2\,\pi}{M}\,\cdot}\right)(t) \\ &= \sum_{k=-\infty}^{\infty} \mathrm{e}^{\mathrm{j}\,\frac{2\,\pi}{M}\,k}\,\underbrace{(\beta_{(\mathrm{j}\,\frac{2\,\pi}{M})} * \beta_{(0,-\mathrm{j}\,\frac{2\,\pi}{M})})(t-k)}_{\frac{2\left(1-\cos\frac{2\,\pi}{M}\right)}{\left(\frac{2\,\pi}{M}\right)^2}\,\varphi(t-\frac{3}{2}-k)},\end{aligned}$$

where we have used the definition of φ from (8), along with the fact that the convolution operator commutes with the shift operator. To simplify the left-hand side, we invoke an important property of linear shift-invariant (LSI) systems: complex exponentials are eigenfunctions of LSI operators. By virtue of this property, if the complex exponential $\mathrm{e}^{\mathrm{j}\,\alpha\,t}$ is presented at the input of a system specified by the impulse response h, then its output is given by $\hat{h}(\alpha)\,\mathrm{e}^{\mathrm{j}\,\alpha\,t}$, where $\hat{h}$ denotes the Fourier transform of h. If we consider $\beta_{(0,-\mathrm{j}\,\frac{2\,\pi}{M})}$ as the impulse response of a LSI system, then

$$\left(\beta_{(0,-\mathrm{j}\,\frac{2\,\pi}{M})} * \mathrm{e}^{\mathrm{j}\,\frac{2\,\pi}{M}\,\cdot}\right)(t) = \underbrace{\hat{\beta}_{(0,-\mathrm{j}\,\frac{2\,\pi}{M})}(\omega)\Big|_{\omega=\frac{2\,\pi}{M}}}_{\lambda}\,\mathrm{e}^{\mathrm{j}\,\frac{2\,\pi}{M}\,t}.$$

Therefore, we have that

$$\mathrm{e}^{\mathrm{j}\,\frac{2\,\pi}{M}\,t} = \sum_{k=-\infty}^{\infty} \mathrm{e}^{\mathrm{j}\,\frac{2\,\pi}{M}\,k}\,2\,\frac{1-\cos\frac{2\,\pi}{M}}{\lambda\,\left(\frac{2\,\pi}{M}\right)^2}\,\varphi(t-\frac{3}{2}-k).$$

By flipping the sign of α we can easily obtain an analogous result for the reproduction of $\mathrm{e}^{-\mathrm{j}\,\frac{2\,\pi}{M}\,t}$. Finally, by using both results, we have that

$$\cos\left(2\,\pi\left(t+\frac{3}{2\,M}\right)\right) = \sum_{k=-\infty}^{\infty} c_1[k]\,\varphi(M\,t-k) \tag{19}$$

$$\sin\left(2\,\pi\left(t+\frac{3}{2\,M}\right)\right) = \sum_{k=-\infty}^{\infty} c_2[k]\,\varphi(M\,t-k) \tag{20}$$

where

$$\begin{aligned}c_1[k] &= \frac{2\,\left(1-\cos\frac{2\,\pi}{M}\right)\,\cos\frac{\pi\,(2\,k+3)}{M}}{\cos\frac{\pi}{M}-\cos\frac{3\,\pi}{M}} \\ c_2[k] &= \frac{2\,\left(1-\cos\frac{2\,\pi}{M}\right)\,\sin\frac{\pi\,(2\,k+3)}{M}}{\cos\frac{\pi}{M}-\cos\frac{3\,\pi}{M}}.\end{aligned}$$

Note that the sequences c_1 and c_2 are M-periodic and that the summations in (19) and (20) can be reduced to finite ones if we make use of the periodized basis functions.

We have expressed in (19) and (20) how to compute the vector coefficients for reproducing sinusoids of unit period and initial phase of $\frac{3\,\pi}{M}$. The appropriate linear combination of c_1 and c_2 then allows one to reproduce sinusoids of arbitrary shape.

IV. Implementation

Since the presented parametric active contour is a spline snake, it is capable of handling all traditional energies applicable to point-snakes and parametric snakes. However, to illustrate the behavior of our parameterization in a real implementation, we performed our experiments with a specific snake energy that we designed to be versatile.

In this section, we first introduce the snake energy that drives the optimization process, and then we provide a description of the implementation details for the proposed snake. We construct the energy functional to detect dark objects on a brighter background.

A. Snake Energy

The active-contour algorithm is always driven by a chosen energy function. Thus, the quality of the segmentation depends on the choice of this energy term. There are many construction strategies which can be categorized in two main families: 1) edge-based schemes, which use gradient information to detect contours [4], [7], [10] and 2) region-based methods, which use statistical information to distinguish different homogeneous regions [9], [35]. In order to benefit from the advantages of both strategies, a unified energy was proposed in [3]. In our case, we are going to follow a similar approach by using a convex combination of gradient and region energies, like in

$$E = \alpha\, E_{\text{edge}} + (1-\alpha)\; E_{\text{region}} \tag{21}$$

where $\alpha \in [0,1]$. The tradeoff parameter α balances the contribution of the edge-based energy and the region-based energy. Its value depends on the characteristics of each particular application.

For the gradient-based (or edge) energy, we consider the one described in [35] since it has the advantage of penalizing the snake when the orientation is inconsistent with the object to segment. Let $\mathbf{r}$ be our parametric snake. The contour energy term is then given by

$$E_{\text{edge}} = -\oint_{\mathbf{r}} \mathbf{k}^{\mathsf{T}}\; (\boldsymbol{\nabla} f(x_1,x_2) \times \mathrm{d}\mathbf{x})\,,$$

where $\mathrm{d}\mathbf{x}$ denotes the tangent vector of the curve in the three-dimensional space formed by the image plane and its orthogonal dimension, where $\mathbf{k} = (0,0,1)$ denotes the outward vector orthonormal to the image plane, where $\boldsymbol{\nabla} f(x_1,x_2) = \left(\frac{\partial f(x_1,x_2)}{\partial x_1}, \frac{\partial f(x_1,x_2)}{\partial x_2}, 0\right)$ is the within-plane gradient of the image f at (x_1,x_2) on the curve, and where $\times$ is the 3D cross product. In Figure 4, we present the configuration of the various quantities involved. The chirality of the system of coordinates will determine the sign of the integrand, as discussed in [3], [35]. Using Green's theorem, the edge energy can be also expressed as the surface integral

$$E_{\text{edge}} = -\int_{\Omega} \Delta f(\mathbf{x})\, \mathrm{d}x_1\, \mathrm{d}x_2, \tag{22}$$

where $\mathbf{x} = (x_1,x_2)$, Δf is the Laplacian of the image f, and Ω is the region enclosed by $\mathbf{r}$.

For the region-based energy, we adopt a strategy similar to [28]. More precisely, our region-based energy discriminates an object from its background by building an ellipse $\mathbf{r}_\lambda$ around the snake and maximizing the contrast between the intensity of the data averaged within the curve, and the intensity of the data averaged over the elliptical shell Ω_λ. When $\Omega \subset \Omega_\lambda$, the region energy term can be expressed as

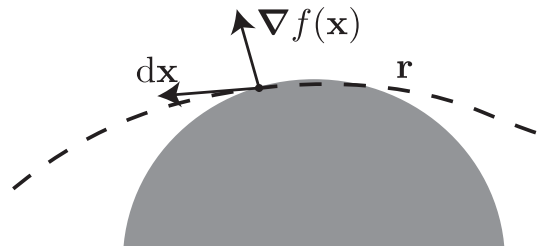

Fig. 4. Schematic representation of a parametric snake $\mathbf{r}$ (dashed line), of its interaction with an object constituted by a gray semicircle (representing low pixel values), of the vector $\mathrm{d}\mathbf{x}$ tangent to the curve, and of the gradient vector $\boldsymbol{\nabla} f$ of the image. The vector $\mathbf{k}$, which is mentioned in the text, is perpendicular to the image plane and points outwards, towards the reader

$$\begin{aligned} E_{\text{region}} \;=\; & \frac{1}{|\Omega|}\left(\int_{\Omega} f(\mathbf{x})\, \mathrm{d}x_1\, \mathrm{d}x_2 \right. \\ & \left. - \int_{\Omega_\lambda \setminus \Omega} f(\mathbf{x})\, \mathrm{d}x_1\, \mathrm{d}x_2\right), \end{aligned} \tag{23}$$

where $|\Omega|$ is given by

$$|\Omega| = -\sum_{k=0}^{M-1}\sum_{n=0}^{M-1} c_1[k]\, c_2[n] \int_0^M \varphi_M(t-n)\, \dot{\varphi}_M(t-k)\, \mathrm{d}t.$$

The normalization factor $|\Omega|$ can be interpreted as the signed area, defined as $|\Omega| = -\oint_{\mathbf{r}} x_2\, \mathrm{d}x_1$. The sign of the quantity $|\Omega|$ depends on the clockwise or anti-clockwise path followed on the curve $\mathbf{r}$. In this paper, we follow the usual convention whereby an anti-clockwise path leads to a positive sign. We enforce our criterion to remain neutral ($E_{\text{region}} = 0$) when f takes a constant value, for instance in flat regions of the image. To achieve this we set $|\Omega_\lambda| = 2\,|\Omega|$.

The construction of the elliptic shell is performed using the best ellipse $\mathbf{r}_{\text{e}}$ given in (17), and magnifying its axes by a factor λ to achieve

$$\begin{aligned} \mathbf{r}_\lambda(t) \;=\; & \mathbf{R}[0] + \lambda\,(\mathbf{R}[1] + \mathbf{R}[-1])\,\cos(2\,\pi\, t) \\ & + \mathrm{j}\,\lambda\,(\mathbf{R}[1] - \mathbf{R}[-1])\,\sin(2\,\pi\, t)\,, \end{aligned}$$

where $\lambda = \sqrt{2\,|\Omega|\,/\,|\Omega_{\text{e}}|}$ and $|\Omega_{\text{e}}|$ is the signed area enclosed by the curve $\mathbf{r}_{\text{e}}$, with

$$|\Omega_{\text{e}}| = -\frac{4\,\pi}{M^2}\cos\frac{\pi}{M}\sum_{k=0}^{M-1}\sum_{n=0}^{M-1} c_1[k]\, c_2[n]\,\sin\frac{2\,\pi\,(n-k)}{M}.$$

In Figure 5, we illustrate how we take advantage of the ideas presented in Section III-D to build the best ellipse approximation $\mathbf{r}_{\text{e}}$ of an arbitrary snake $\mathbf{r}$. Using the constraint $|\Omega_\lambda| = 2\,|\Omega|$, we can determine the contour $\mathbf{r}_\lambda$ of the enclosing shell Ω_λ.

B. Accelerated Implementation

The computational cost is dominated by the evaluation of the surface integrals in (22) and (23). An efficient way to implement these operations is the use of pre-integrated images. Let g be the function we are integrating (Δf, f, or $-f$,

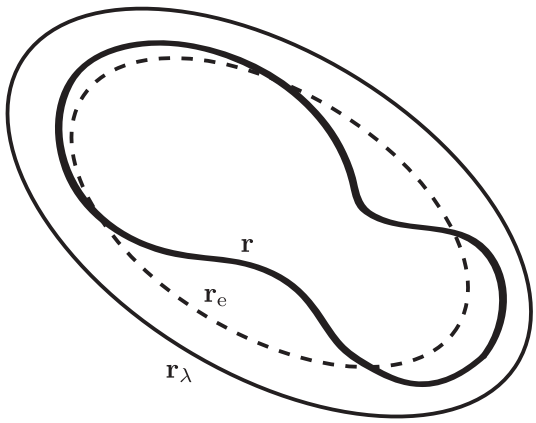

Fig. 5. Representation of the parametric snake $\mathbf{r}$, the best ellipse approximation $\mathbf{r}_{\mathrm{e}}$, and the corresponding enclosing shell $\mathbf{r}_\lambda$ used in E_{region}.

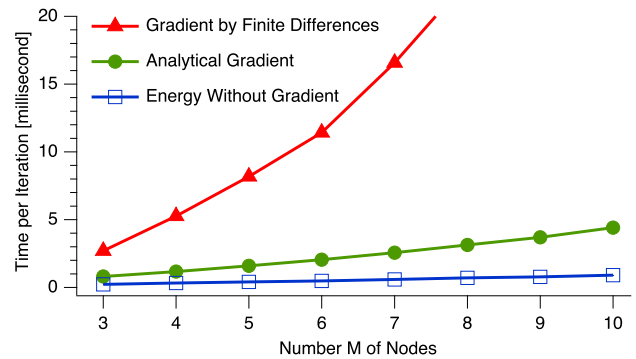

Fig. 6. Mean time of one iteration in the snake evolution.

respectively) and let Γ be the domain of integration (Ω or Ω_λ). Then, by Green's theorem, we rewrite the surface integrals as the line integrals

$$\begin{aligned}\int_\Gamma g(\mathbf{x})\,\mathrm{d}x_1\,\mathrm{d}x_2 &= -\oint_{\partial\Gamma} g_2(x_1,x_2)\,\mathrm{d}x_1\\ &= \oint_{\partial\Gamma} g_1(x_1,x_2)\,\mathrm{d}x_2,\end{aligned}$$

where $\partial\Gamma$ is the boundary of Γ, and

$$g_2(x_1,x_2) = \int_{-\infty}^{x_2} g(x_1,\xi_2)\,\mathrm{d}\xi_2 \tag{24}$$

$$g_1(x_1,x_2) = \int_{-\infty}^{x_1} g(\xi_1,x_2)\,\mathrm{d}\xi_1. \tag{25}$$

The use of Green's theorem to rewrite the surface integrals as line integrals reduces dramatically the computational load. This can only be achieved if the curve is defined continuously, like with the curves of Section II-A. By contrast, this acceleration would not be available to methods such as point-snakes and level-sets, because their implementation ultimately relies on discretization.

C. Sampling

Despite the fact that we are assuming a continuously defined model for our functions, in a real-world implementation we only have at our disposal a sampled version of the functions we want to pre-integrate. To solve this inconsistency, we perform a bilinear interpolation of the sampled data and we store in lookup tables the values of (24) and (25) at integer locations. Then, the energies are obtained using the first approximation given by the lookup tables. In our implementation, we have corrected them by supplying a residual that allows us to get the exact result. We were able to determine this residual analytically but, in the interest of space, we do not provide it here.

D. Optimization

The optimization of the snake can be efficiently carried out by Powell-like line-search methods [36]. These methods require the derivatives of the energy function with respect to the parameters (*i.e.*, the knot coefficients), and converge quadratically to the solution. The algorithm proceeds as follows: firstly, one direction within the parameter space is chosen depending on the partial derivatives of the energy. Secondly, a one-dimensional minimization is performed within the selected direction. Finally, a new direction is chosen using the partial derivatives of the energy function once more, while enforcing conjugation properties. This scheme is repeated till convergence. Assuming a bilinear interpolation of the original function f, we were able to derive exact and closed expressions for these derivatives that take the residual of the lookup table into account.

For spline snakes it has been shown that the evaluation of the partial derivatives of the energy of the form (21) depends quadratically on the number of parameters [3]. In Figure 6, we compare the computational cost of the snake during line minimization (simple update), and when the energy gradient is required to chose a new direction (gradient update). For the latter case, we contrast the computation time of an analytical computation of the gradient to that of a centered finite differences approach. For low values of M, the simple update and the gradient update using analytical energy gradient lead to a similar computational load. As the value of M increases, the quadratic behavior of the computation of the gradient makes the update cost increase. This quadratic behavior can be easily discerned in the topmost curve of Figure 6.

V. Experiments

We present in this section four experimental setups. In the first one, we compare our choice in (8) against the classical quadratic B-spline when representing sinusoids. We move away from sinusoids in the second experiment, where we work with synthetic data and perform an objective validation of the segmentation properties of our snake in noiseless and noisy environments. In the fourth setup, we also perform a quantitative evaluation by segmenting real cardiac MRI data. Finally, in the last experiment, we illustrate some real applications of our snake where the ground truth is not available.

A. Approximation of Sinusoids

By design, our basis function φ has the property of reproducing sinusoids exactly. By contrast, the classical polynomial

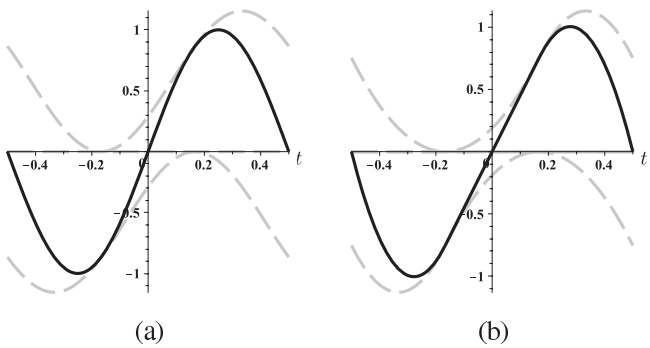

Fig. 7. Approximations of a $\sin$ function with unit period. (a) Parametric representation (solid line) using φ_3 (dashed lines). (b) Best parametric approximation (solid line) using β^2 (dashed lines).

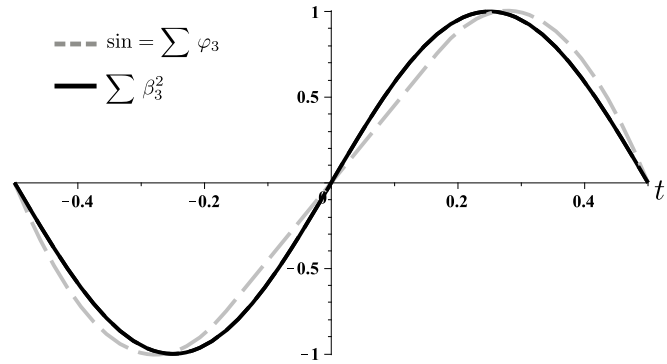

Fig. 8. Sinusoid of period 3, its representation with our basis function (solid line), and its best quadratic B-spline approximation (dashed line).

B-splines do not enjoy this property. In this section, we are focusing on this aspect and exhibit the amount of error committed by B-splines when attempting to reproduce a $\sin$ function.

We start with exact reproduction by our basis. Using the result of Section III-E, we determine the coefficients for the case $M = 3$ (smallest possible M). They are given by

$$\sin(2\pi t) = \sqrt{3}\,\left(\varphi_3(3t-1) - \varphi_3(3t+1)\right),$$

where φ_3 corresponds to the 3-periodization of the basis function (8), as in (2).

We continue with approximate reproduction by B-splines. For fairness, we choose a quadratic B-spline β^2 so that the size of the support of β^2 and φ is the same. The reproduction will be approximate, not because of the limited size of the support, but because the $\sin$ function does not lie in the span of polynomial B-splines of any degree. Nevertheless, we can compute the coefficients that best adjust the sinusoid with unit period in the least-squares sense. This yields

$$\sin 2\pi t \approx \frac{1215}{26\pi^2}\,\left(\beta_3^2(3t-1) - \beta_3^2(3t+1)\right),$$

where

$$\beta^2(t) = \begin{cases} \frac{3}{4} - |t|^2 & 0 \le |t| < \frac{1}{2} \\ \frac{1}{2}\left(\frac{3}{2} - |t|\right)^2 & \frac{1}{2} \le |t| < \frac{3}{2} \\ 0 & \frac{3}{2} \le |t| \end{cases} \tag{26}$$

is the quadratic B-spline and the subscript 3 indicates a 3-periodized basis function as in (2).

We observe in Figure 7 that both constructions result in sine-like functions. However, the reproduction is exact in the left part of Figure 7, while it is only approximate in the right part. This happens even though the support of β^2 is identical to the support of φ, even though the asymptotic approximation properties of β^2 and φ are identical, and even though β^2 and φ have the same degree of differentiability. We show in Figure 8 the amount of error committed by the parabolic approximation. We determine that $\mathrm{MSE} = \frac{1}{2} - \frac{98415}{208\,\pi^6}$.

B. Accuracy and Robustness to Noise

In this section, two experiments are carried out. The first one consists in outlining different synthetic blob-like shapes in a noise-free environment. The second experiment consists in outlining one specific target within an image, this time, in the presence of noise. In both experiments we set $\alpha = 0$, that is, we make use of the region energy only. This particular choice ensures that the snake is not mislead by noisy boundaries in the presence of excessive of noise.

In the first experiment, we generate 10 test images of size (512×512) by pixel-wise sampling of our shape of interest, which is built by intersecting or making the union of two circles of radius 50 pixel units. We illustrate these shapes in the header of Table I. They are parameterized with the distance d, in pixel units, between the centers of the circles. For $d < 0$, the shape is built by the intersection of the two circles. For $d \ge 0$, they are parameterized by their union. The grayscale values of the images are 255 for the shape, and 0 for the background.

We used the Jaccard distance $J = 1 - |\Theta \cap \Omega| \,/\, |\Theta \cup \Omega|$ to measure as a percentage the dissimilarity between the two sets. There, Θ corresponds to the ground-truth region, and Ω corresponds to the region enclosed by the snake. We computed J with a pixel-wise discretization of the images.

In the simulations of Table I, we investigated the dependence of J on the number M of coefficients and the distance d between the circles. We denoted with a dash $(-)$ when the snake did not converge, and therefore, we could not compute the Jaccard distance. We initialized every snake as a circle with a radius of 75 pixel and a center that lay in the middle of the shape. We observe that the results in Table I tend to improve as the number M of control points is increased, especially for the non-elliptical shapes. However, the increase in the number of control points does not bring any further improvement when the shape to segment is a perfect circle. This result is expected since the circular shape is reproduced exactly for any $M \ge 3$. The residual error seen in Table I for $d = 0$ can be attributed to the discretization of Θ and Ω. We also observe that for $d = -80$ and $d = -64$ the Jaccard distance starts increasing severely for $M \ge 7$ and for $M \ge 9$, respectively. This is due to the fact that the sharp corners of the shape lead to loops in the curve during the optimization process. Such self-intersections violate the conditions of Green's theorem in Section IV-A.

In the second experiment, we investigated the sensitivity

M	$d=-80$	$d=-64$	$d=-48$	$d=-32$	$d=-16$	$d=0$	$d=16$	$d=32$	$d=48$	$d=64$
3	5.08	4.12	3.78	2.84	1.54	0.17	2.18	4.06	6.63	9.49
4	4.85	4.12	3.84	2.78	1.53	0.15	2.22	4.01	6.64	9.48
5	3.53	2.64	2.03	1.25	0.58	0.20	1.06	2.27	4.21	6.82
6	2.69	2.18	2.00	1.13	0.64	0.17	0.91	1.81	2.84	4.36
7	3.63	1.87	1.63	1.08	0.48	0.17	1.09	1.92	2.50	3.68
8	18.84	0.58	0.68	0.55	0.32	0.18	0.86	1.92	4.00	5.73
9	–	1.56	0.99	0.72	0.30	0.15	0.55	0.85	1.41	–
10	–	1.41	0.93	0.70	0.34	0.17	0.18	0.41	0.80	1.23

TABLE I
ERROR PERCENTAGE OF OUR SNAKE FOR NOISELESS SYNTHETIC DATA.

M	SNR= 15dB	SNR= 10dB	SNR= 5dB	SNR= 0dB	SNR= -5dB	SNR= -10dB
3	100	100	100	100	99	45
4	100	100	100	100	96	33
5	99	99	100	100	97	25
6	100	99	100	99	98	25
7	100	99	100	99	90	20
8	99	100	100	98	90	7
9	99	98	99	96	92	7
10	96	99	97	100	92	11

TABLE II
PERCENTAGE OF SUCCESS RATE OF OUR SNAKE FOR NOISY SYNTHETIC DATA.

to noise of our snake depending on the number of snake coefficients M. We generated 100 noisy realizations of a circle of radius 50 pixel units for different signal-to-noise ratios. We computed the power of the noise over a region of interest of size (200×200). We illustrate a realization of the resulting images in the header of Table II.

We show the percentage of success in Table II. We considered that our snake succeeded in segmenting the circle when the optimization process led to a segmentation with $J < 1\%$. This criterion is very conservative as shown in Figure 9. We observe from the results that our snake is robust against noise since it is capable of giving a proper segmentation even for low signal-to-noise ratios. Furthermore, the increased sensitivity to noise as we increase the number of vector coefficients M corresponds to the appearance of additional noise-related local minima in the energy of the snake. Therefore, M should be chosen as small as possible in order to avoid over-fitting of the noise, but big enough to be able to approximate the shape of interest.

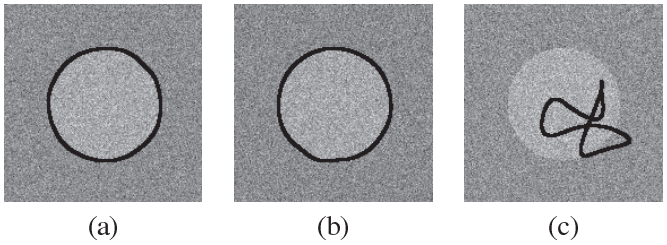

Fig. 9. Segmentation results for noisy synthetic data with SNR= -5dB. (a) Barely accepted with J= 0.853%. (b) Barely rejected with J= 1.001%. (a) Rejected with J= 81.065%.

C. Medical Data

Now, we move away from synthetic data. We compare our snake against other snake variants in terms of accuracy and speed. We quantify their accuracy at outlining the endocardial wall of the left ventricle within slices of 3D cardiac MR image sequences.

The data we used are short-axis cardiac MR image sequences from 33 subjects acquired in the Department of Imaging of the Hospital for Sick Children in Toronto, Canada [37]. For each subject, data consist of a time-series of 20 volumes. For each volume, the number of slices varies from 8 to 15. Each slice is a (256×256) image with a pixel spacing between 0.93 mm and 1.64 mm. The ground truth was obtained by manual annotation. In each segmented image 1,000 points (named *landmark points*) define a closed polygon outlining the endocardial wall.

1) Accuracy: For each subject, we selected one slice guided by its anatomical structures along the long axis and its timing in the cardiac cycle. Since the region of interest is nearly elliptical, we used the minimalistic elliptical active contour named Ovuscule to provide a first estimate of the location and orientation of the left ventricle [28]. Then, we refined the segmentation of the endocardial wall using the general parametric active contour model (1) for different values of M and several basis functions. More specifically, we used linear

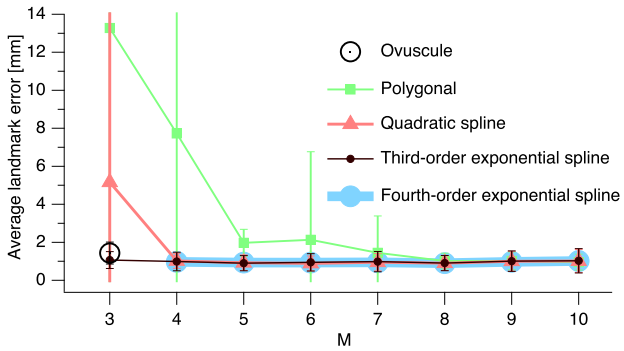

Fig. 10. Mean and variance of the landmark error across all 33 patients.

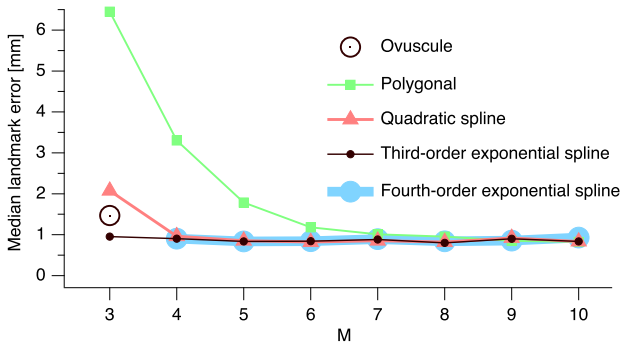

Fig. 11. Median of the landmark error across all 33 patients.

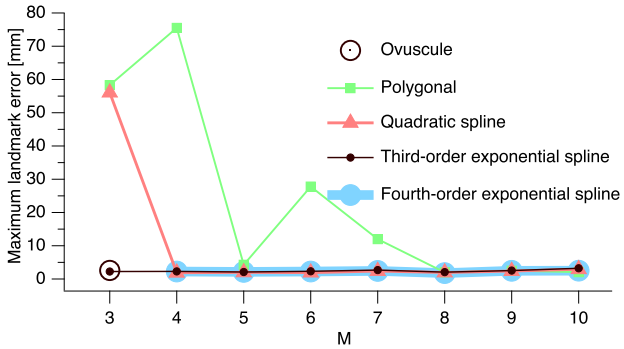

Fig. 12. Maximum landmark error among all 33 patients.

and quadratic B-splines, our function (8) that we refer to as third-order exponential spline, and an extended version of (8) that we refer to as fourth-order exponential spline. The linear B-spline basis function has a smaller support than our function (8). However, it can only adopt the form of polygons. The quadratic B-spline basis function has the same support and regularity than (8). However, it is unable to reproduce ellipses. Finally, the fourth-order exponential spline is an extended version of (8), with one more degree of regularity, but with a support one unit larger. The initialization provided by the Ovuscule could be carried over to (8) and to the fourth-order exponential spline. In the case of the other types of snake, the perfect ellipse of the Ovuscule cannot be reproduced but must be approximated. This approximation was achieved by sampling the outline of the Ovuscule.

In a preprocessing step, the images were magnified four times horizontally and vertically. Firstly, we evolved the Ovuscule on the magnified image. Secondly, we evolved more refined snakes, guided exclusively by the edge energy on a smoothed version of the magnified image. The smoothing was Gaussian, with a kernel of variance $\sigma^2 = 10^2$. We then measured the landmark error. We computed this error as the mean distance of the snake to the landmark points given by the ground truth, as was done in [37].

In Figures 10, 11, and 12, we show the mean, median, and maximum values of the landmark error, respectively. From these graphs, we validate that the Ovuscule provides a good and robust starting point to be refined by the snakes investigated in this paper. The polygonal snake does not reach the accuracy of the Ovuscule till $M = 7$, and exhibits a high variance across subject. The quadratic-spline snake and the third-order exponential-spline snake converge to similar accuracy starting with $M = 4$. This was expected, since we showed in Section III-B that our function does converge to a quadratic B-spline when M increases. However, for low values of M, the difference is noticeable, and the quadratic-spline snakes produce shapes that are not compatible with the region of interest. Finally, the fourth-order exponential-spline snakes produce equivalent results in terms of accuracy and stability than the third-order exponential-spline snake, at a price of a larger support, and therefore, of a slower convergence.

In Figure 13b, we illustrate the initialization provided to the Ovuscule, and in Figure 13c the outcome of optimizing the Ovuscule, which will provide the initialization for further processing. We also show the result of several more elaborated snake variants, and how they compare with the ground truth. The fourth-order exponential-spline snake results in an outline that is visually indistinguishable from that of the third-order one, but comes at an increased computational cost.

2) Speed: In terms of speed, we compared our proposed snake to some classic traditional snakes such as a Kass-like snake [38] and a traditional Geodesic Active Contour (GAC) model [13].

In this analysis, we used the anatomical structures of the 33 patients found in Section V-C1. However, we modified our initialization procedure to accommodate for the GAC model, since it fails unless the initial contour lies totally inside or outside of the boundary of interest. Therefore, we scaled down the initialization that was provided by the outcome of optimizing an Ovuscule in Section V-C1. By doing so, we guarantee that all initial contours lay inside the endocardial wall to segment. Unfortunately, neither the Kass-like snake nor the GAC model are able to reproduce the initial ellipse perfectly and their initialization must be approximated. This approximation was achieved by sampling the outline of the Ovuscule. Finally, we refined the segmentation of the endocardial wall either using our snake model for different values of M, the Kass-like snake, or the GAC.

This experiment was performed on a MacPro 3.1 with two Quad-Core Intel Xeon processors and 8GB of RAM memory running Mac OS X 10.6.8. The implementation of the Kass-like active contour was taken from [38], and the one of GAC model from the free open-source image processing package

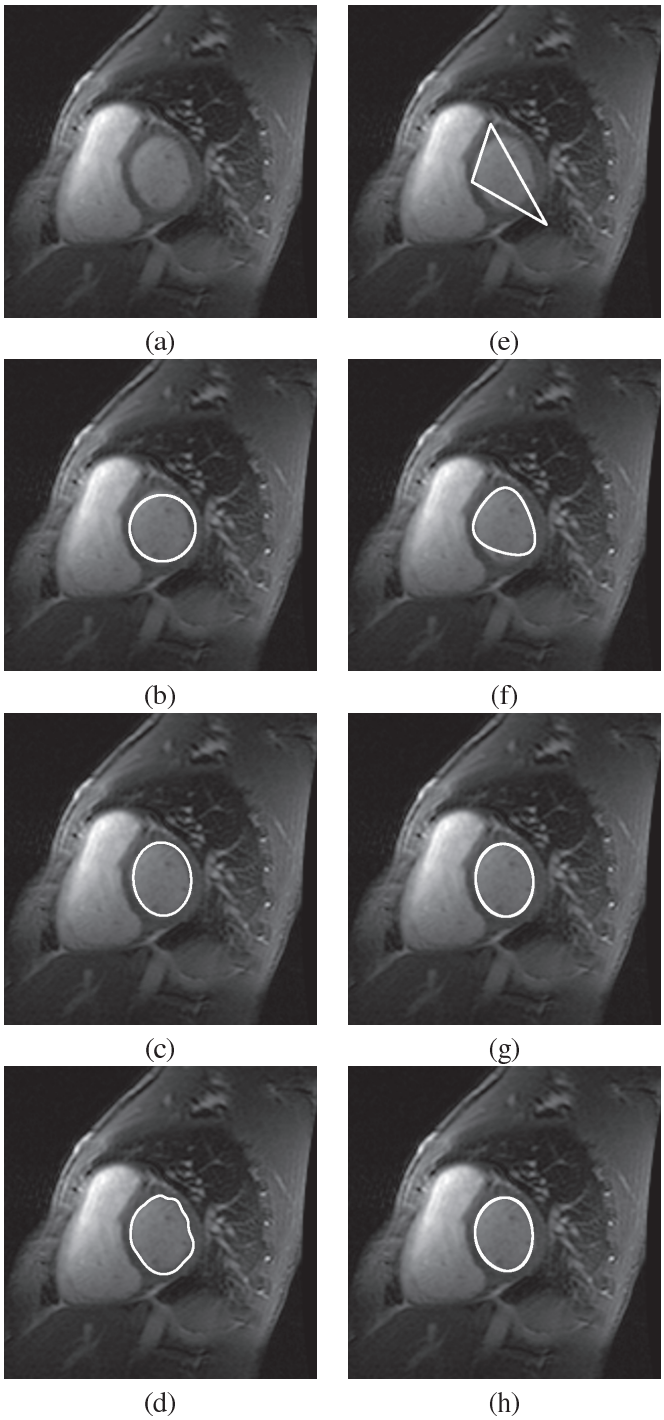

Fig. 13. Outline of the endocardial wall in the first frame and fourth slice of the second patient. (a) Raw data. (b) Initialization. (c) Ovuscule. (d) Ground truth. (e) Polygonal snake with $M = 3$. (f) Quadratic-spline snake with $M = 3$. (g) Third-order exponential-spline snake with $M = 3$. (h) Fourth-order exponential-spline snake with $M = 4$.

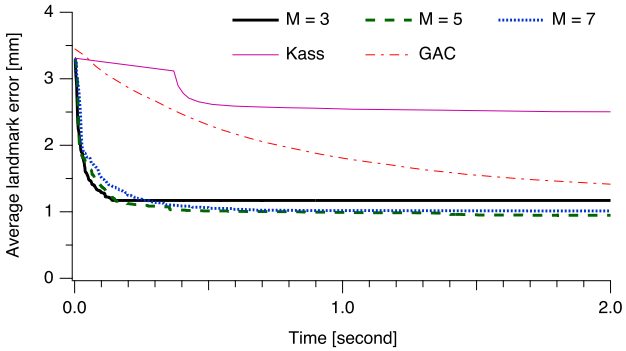

Fig. 14. Temporal evolution of the Jaccard distance. During the 2 seconds of snake evolution, the proposed method with $M = 3$ performed 1479 iterations, with $M = 5$ it performed 1406 iterations, and with $M = 3$ it performed 889 iterations. The Kass snake performed 17 iterations, the first of which took 370ms, and the GAC performed 34 iterations.

Fiji[1] implementing the algorithm described in [13].

In Figure 14, we show the mean temporal evolution of the improvement of the Jaccard distance during the snake evolution process for the 33 patients. We can clearly see that the proposed snake reaches its optimum earlier than the classical Kass-like snake and the GAC model. The Kass-like snake has a very costly first step, and then it cannot escape a local minimum. The GAC is executed with an advection value of 2.20, and a propagation value of 1. These parameters make the GAC succeed in overcoming the local minimum, but the convergence rate is still slower than that of the parametric case. It is important to notice that, for our proposed model, an increase in the number M of control points slows the convergence. As pointed out in Section IV-D, this is due to the fact that larger values of M increase the computational load per iteration of the snake.

D. Real Data

Here, we illustrate the behavior of our snake and provide further insights into its capabilities. In the context of this section, the ground truth is missing, so we must relinquish quantitative assessments in favor of qualitative ones.

1) HeLa Nuclei: We want to evaluate the success of our snake model at outlining ellipse-like targets in the context of automated time-lapse microscopy. We use (434×434) images of HeLa nuclei that express fluorescent core histone 2B on an RNAi live cell array. We show in Figure 15 the result of the optimization process with (8) and $M = 5$. This number of points is high enough to capture small departures from an elliptic shape.

We initialized every snake as a circle of radius of 25 pixel units, as shown in Figure 15. These initial circles were centered on the locations given by a maxima detector applied over a version of the image that was smoothed with a Gaussian kernel of variance $\sigma^2 = 12^2$ pixel. A total number of 23 maxima were detected. We then proceed with an inverted version of the original, unsmoothed image to optimize the snakes. The optimization process converged in 22 cases. We

[1]http://fiji.sc/

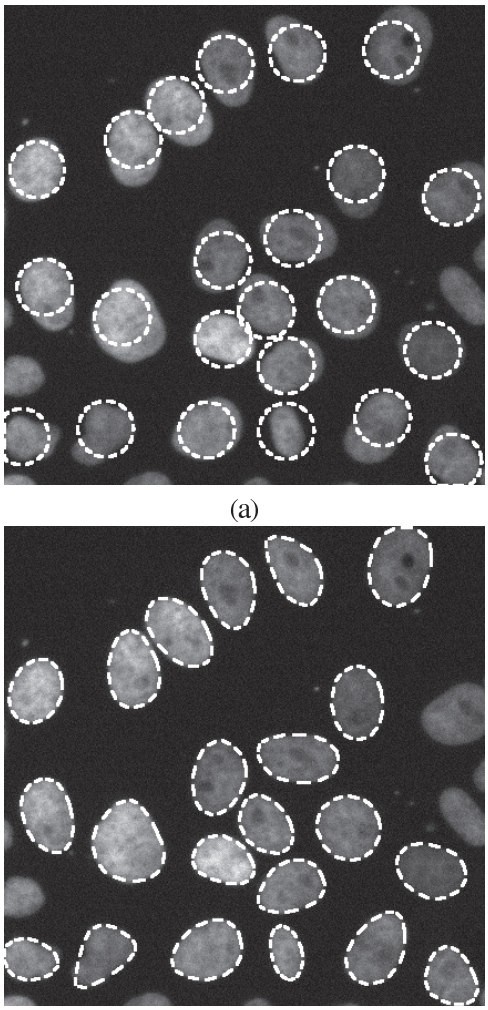

Fig. 15. Outline of HeLa nuclei in a fluorescence microscopy image. The parametric snakes were built with $M = 5$. (a) The initial contour of the snake. (b) Result provided by our snake.

show in Figure 15 the result of the outlining process. We observe that our snakes were successful in most of the cases.

2) Droplets: As a second example, we show the outline of sprayed and deformed water droplets hitting a surface. The flight and the impact of the droplet was captured by a high-speed camera (Photron Fastcam) at a rate of 10,000 images/s. The shape of the droplet is changing during flight, at impact, and while bouncing. After cropping, the size of the image was (663×663) pixels.

We analyzed two frames. One was an image taken before the collision took place, the other was taken after the impact. In both cases, we initialized the snake as a circle with a position and size that we chose manually. These initializations are shown in Figure 16. In the image prior to the impact, which we show in the left part of Figure 16, a snake with $M = 5$ was used. We selected a small value for M because the droplet is nearly circular. In the image after the impact, which we show in the right part of Figure 16, five control points did not provide enough freedom to cope with the discontinuity created by the attachment to the surface. However, the outline

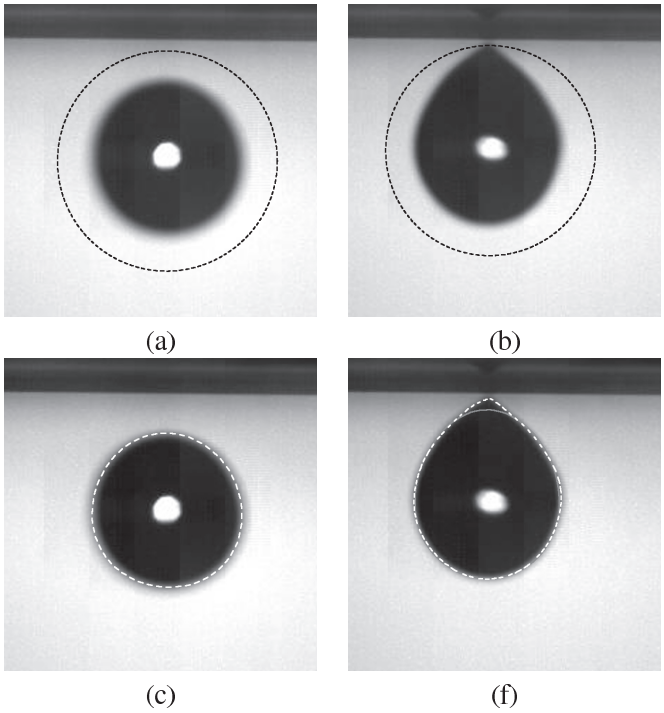

Fig. 16. Sprayed droplets. (a) Prior to the impact: The initial contour of the snake is is represented with a black dashed line. (b) After the impact: The initial contour of the snake is is represented with a black dashed line. (c) Prior to the impact: The outline of our snake with $M = 5$ is represented with a white dashed line. (d) After the impact: The outline of the successful snake is is represented with a white dashed line ($M = 8$), while the configuration with $M = 5$ is represented with a gray solid line. The droplet edges are partially out of focus, making them blurry and noisy.

was successfully retrieved when slightly increasing the number of nodes to $M = 8$.

The method described in this article has been programmed as a plugin for ImageJ, which is a free open-source multi-platform Java image-processing software[2]. Our plugin[3] is independent of any imaging hardware and, thanks to ImageJ, any common file format may be used.

VI. Conclusions

Our contribution in this paper is a new family of basis functions that we use to describe parametric contours in terms of a set of control points. We were able to single out the basis of shortest support that allows one to reproduce circles and ellipses. Those can be characterized exactly by as few as three control points but, by considering additional ones, our parametric contours can reproduce with arbitrary precision any planar closed curve. In particular, we have shown that the mean error of approximation decays in inverse proportion of the cube of the number of control points. We have used our ellipse-reproducing parametric curves to build snakes driven by a combination of contour and region-based energies. In the latter case, the energy depends on the contrast between two regions, one being delineated by the curve itself, and the other by an ellipse of double area. To determine this ellipse, we showed

[2]http://rsb.info.nih.gov/ij/

[3]http://bigwww.epfl.ch/algorithms/esnake/

how to compute the best elliptical approximation, in a least-squares sense, of a contour described by an arbitrary number of control points. We were able to accelerate the implementation of our snakes by taking advantage of Green's theorem, which was facilitated by the availability of the explicit expressions of our basis. We have applied our snakes to a variety of problems that involve synthetic simulations and real data. We achieved excellent objective and subjective performance.

REFERENCES

[1] T. McInerney and D. Terzopoulos, "Deformable Models in Medical Image Analysis: A Survey," *Medical Image Analysis*, vol. 1, no. 2, pp. 91–108, 1996.

[2] A. Jain, Y. Zhong, and M.-P. Dubuisson-Jolly, "Deformable Template Models: A Review," *Signal Processing*, vol. 71, no. 2, pp. 109–129, 1998.

[3] M. Jacob, T. Blu, and M. Unser, "Efficient Energies and Algorithms for Parametric Snakes," *IEEE Transactions on Image Processing*, vol. 13, no. 9, pp. 1231–1244, September 2004.

[4] M. Kass, A. Witkin, and D. Terzopoulos, "Snakes: Active Contour Models," *International Journal of Computer Vision*, vol. 1, no. 4, pp. 321–331, 1987.

[5] C. Xu and J. Prince, "Snakes, Shapes, and Gradient Vector Flow," *IEEE Transactions on Image Processing*, vol. 7, no. 3, pp. 359–369, March 1998.

[6] J. Gao, A. Kosaka, and A. Kak, "A Deformable Model for Human Organ Extraction," in *Proceedings of the 1998 IEEE International Conference on Image Processing (ICIP'98)*, vol. 3, October 4-7, 1998, pp. 323–327.

[7] L. Staib and J. Duncan, "Boundary Finding with Parametrically Deformable Models," *IEEE Transactions on Pattern Analysis and Machine Intelligence*, vol. 14, no. 11, pp. 1061–1075, November 1992.

[8] A. Chakraborty, L. Staib, and J. Duncan, "Deformable Boundary Finding in Medical Images by Integrating Gradient and Region Information," *IEEE Transactions on Medical Imaging*, vol. 15, no. 6, pp. 859–870, December 1996.

[9] M. Figueiredo, J. Leitão, and A. Jain, "Unsupervised Contour Representation and Estimation Using B-Splines and a Minimum Description Length Criterion," *IEEE Transactions on Image Processing*, vol. 9, no. 6, pp. 1075–1087, June 2000.

[10] P. Brigger, J. Hoeg, and M. Unser, "B-Spline Snakes: A Flexible Tool for Parametric Contour Detection," *IEEE Transactions on Image Processing*, vol. 9, no. 9, pp. 1484–1496, September 2000.

[11] M. Gebhard, J. Mattes, and R. Eils, "An Active Contour Model for Segmentation Based on Cubic B-Splines and Gradient Vector Flow," in *Proceedings of the 2001 Conference on Medical Image Computing and Computer-Assisted Intervention (MICCAI'01)*, vol. 2208/2009, October 14-17, 2001, pp. 1373–1375.

[12] R. Malladi, J. Sethian, and B. Vemuri, "Shape Modeling with Front Propagation: A Level Set Approach," *IEEE Transactions on Pattern Analysis and Machine Intelligence*, vol. 17, no. 2, pp. 158–175, February 1995.

[13] V. Caselles, R. Kimmel, and G. Sapiro, "Geodesic Active Contours," *International Journal of Computer Vision*, vol. 22, no. 1, pp. 61–79, 1997.

[14] K. Zhang, L. Zhang, H. Song, and W. Zhou, "Active Contours with Selective Local or Global Segmentation: A New Formulation and Level Set Method," *Image and Vision Computing*, vol. 28, no. 4, pp. 668–676, April 2010.

[15] K. Zhang, H. Song, and L. Zhang, "Active Contours Driven by Local Image Fitting Energy," *Pattern Recognition*, vol. 43, no. 4, pp. 1199–1206, April 2010.

[16] T. McInerney and D. Terzopoulos, "T-snakes: Topology Adaptive Snakes," *Medical Image Analysis*, vol. 4, no. 2, pp. 73–91, June 2000.

[17] F. Precioso and M. Barlaud, "B-Spline Active Contour with Handling of Topology Changes for Fast Video Segmentation," *EURASIP Journal on Applied Signal Processing*, vol. 2002, no. 6, pp. 555–560, June 2002.

[18] G. Sapiro, *Geometric Partial Differential Equations and Image Analysis*. Cambridge, UK: Cambridge University Press, 2006, First edition, 412 p.

[19] J. Blokland, A. Vossepoel, A. Bakker, and E. Pauwels, "Delineating Elliptical Objects with an Application to Cardiac Scintigrams," *IEEE Transactions on Medical Imaging*, vol. 6, no. 1, pp. 57–66, March 1987.

[20] P. Lipson, A. Yuille, D. O'Keeffe, J. Cavanaugh, J. Taaffe, and D. Rosenthal, "Deformable Templates for Feature Extraction from Medical Images," in *Proceedings of the 1990 First European Conference on Computer Vision Proceedings (ECCV'90)*, vol. 427/1990, Antibes, France, April 23-27, 1990, pp. 0302–9743.

[21] I. Adame, R. Van Der Geest, D. Bluemke, J. Lima, J. Reiber, and B. Lelieveldt, "Automatic Vessel Wall Contour Detection and Quantification of Wall Thickness in In-Vivo MR Images of the Human Aorta," *Journal of Magnetic Resonance Imaging*, vol. 24, no. 3, pp. 595–602, September 2006.

[22] J. Guerrero, S. Salcudean, J. McEwen, B. Masri, and S. Nicolaou, "Real-Time Vessel Segmentation and Tracking for Ultrasound Imaging Applications," *IEEE Transactions on Medical Imaging*, vol. 26, no. 8, pp. 1079–1090, August 2007.

[23] S. Tsuji and F. Matsumoto, "Detection of Ellipses by a Modified Hough Transformation," *IEEE Transactions on Computers*, vol. 27, no. 8, pp. 777–781, August 1978.

[24] N. Bennett, R. Burridge, and N. Saito, "A Method to Detect and Characterize Ellipses Using the Hough Transform," *IEEE Transactions on Pattern Analysis and Machine Intelligence*, vol. 21, no. 7, pp. 652–657, July 1999.

[25] I. Adame, R. van der Geest, B. Wasserman, M. Mohamed, J. Reiber, and B. Lelieveldt, "Automatic Segmentation and Plaque Characterization in Atherosclerotic Carotid Artery MR Images," *Magnetic Resonance Materials in Physics, Biology and Medicine*, vol. 16, no. 5, pp. 227–234, April 2004.

[26] B. Alberts, A. Johnson, J. Lewis, M. Raff, K. Roberts, and P. Walter, *Molecular Biology of The Cell*. New York NY, USA: Garland Science, 2007, Fifth edition, 1601 p.

[27] A. Stalder, G. Kulik, D. Sage, L. Barbieri, and P. Hoffmann, "A Snake-Based Approach to Accurate Determination of Both Contact Points and Contact Angles," *Colloids And Surfaces A: Physicochemical And Engineering Aspects*, vol. 286, no. 1-3, pp. 92–103, September 2006.

[28] P. Thévenaz, R. Delgado-Gonzalo, and M. Unser, "The Ovuscule," *IEEE Transactions on Pattern Analysis and Machine Intelligence*, vol. 33, no. 2, pp. 382–393, February 2011.

[29] M. Unser, "Sampling—50 Years After Shannon," *Proceedings of the IEEE*, vol. 88, no. 4, pp. 569–587, April 2000.

[30] M. Jacob, T. Blu, and M. Unser, "Sampling of Periodic Signals: A Quantitative Error Analysis," *IEEE Transactions on Signal Processing*, vol. 50, no. 5, pp. 1153–1159, May 2002.

[31] A. Aldroubi and M. Unser, "Sampling Procedures in Function Spaces and Asymptotic Equivalence with Shannon's Sampling Theory," *Numerical Functional Analysis and Optimization*, vol. 15, no. 1-2, pp. 1–21, 1994.

[32] R. Delgado-Gonzalo, P. Thévenaz, and M. Unser, "Exponential Splines and Minimal-Support Bases for Curve Representation," *Computer Aided Geometric Design*, 2010, submitted.

[33] M. Unser and T. Blu, "Cardinal Exponential Splines: Part I—Theory and Filtering Algorithms," *IEEE Transactions on Signal Processing*, vol. 53, no. 4, pp. 1425–1438, April 2005.

[34] M. Unser, "Splines: A Perfect Fit for Signal and Image Processing," *IEEE Signal Processing Magazine*, vol. 16, no. 6, pp. 22–38, November 1999.

[35] M. Jacob, T. Blu, and M. Unser, "A Unifying Approach and Interface for Spline-Based Snakes," in *Progress in Biomedical Optics and Imaging, vol. 2, no. 27*, ser. Proceedings of the SPIE International Symposium on Medical Imaging: Image Processing (MI'01), M. Sonka and K. Hanson, Eds., vol. 4322, San Diego CA, USA, February 19-22, 2001, pp. 340–347, Part I.

[36] W. Press, S. Teukolsky, W. Vetterling, and B. Flannery, *Numerical Recipes: The Art of Scientific Computing*. Cambridge, UK: Cambridge University Press, 1986, Third edition, 818 p.

[37] A. Andreopoulos and J. Tsotsos, "Efficient and Generalizable Statistical Models of Shape and Appearance for Analysis of Cardiac MRI," *Medical Image Analysis*, vol. 12, no. 3, pp. 335–357, June 2008.

[38] P. Andrey and T. Boudier, "Adaptive Active Contours," in *First ImageJ User & Developer Conference*, Luxembourg, May 18-19 2006.

Ricard Delgado-Gonzalo was born in 1983 in Barcelona, Spain. He received two diplomas in Telecommunications Engineering and in Mathematics from the Universitat Politècnica de Catalunya (UPC) in 2006 and 2007, respectively. In 2008, he joined the Biomedical Imaging Group at the École polytechnique fédérale de Lausanne (EPFL), Switzerland, as a Ph.D. student and assistant. He currently works on applied problems related to image reconstruction, segmentation, and tracking, as well as on the mathematical foundations of signal processing and spline theory. His other important professional interests include technology management and transfer.

Philippe Thévenaz was born in 1962 in Lausanne, Switzerland. He graduated in January 1986 from the École polytechnique fédérale de Lausanne (EPFL), Switzerland, with a diploma in microengineering. He then joined the Institute of Microtechnology (IMT) of the University of Neuchâtel, Switzerland, where he worked in the domain of image processing (optical flow) and in the domain of speech processing (speech coding and speaker recognition). He obtained his Ph.D. in June 1993, with a thesis on the use of the linear prediction residue for text-independent speaker recognition. He then worked as a Visiting Fellow with the Biomedical Engineering and Instrumentation Program, National Institutes of Health (NIH), Bethesda MD, USA, where he developed research interests that include splines and multiresolution signal representations, geometric image transformations, and biomedical image registration. Since 1998, he is with the EPFL as senior researcher.

Chandra Sekhar Seelamantula (M'99) was born in 1976 in Gollepalem, Andhra Pradesh, India. He obtained a Bachelor of Engineering (B.E.) degree in 1999 with a Gold medal from the University College of Engineering, Osmania University, India, with a specialization in Electronics and Communication Engineering. He obtained a direct Ph.D. degree in 2005 from the Indian Institute of Science, Department of Electrical Communication Engineering, with a thesis titled, Time- varying Signal Models: Envelope and Frequency Estimation with Applications to Speech and Music Signal Compression. During his Ph.D., he also specialized in the development of auditory-motivated signal processing models for speech and audio applications. During April 2005 - March 2006, he worked as a Technology Consultant for M/s. ESQUBE Communication Solutions Private Limited, Bangalore, and developed proprietary audio coding solutions. In April 2006, he joined the Biomedical Imaging Group, École polytechnique fédérale de Lausanne, Switzerland, as postdoctoral fellow and specialized in the field of Image Processing, Optical-Coherence Tomography, Holography, Splines, and Sampling Theories. Since July 2009, he is Assistant Professor at the Department of Electrical Engineering, Indian Institute of Science, Bangalore.

Michael Unser (M'89-SM'94-F'99) received the M.S. (*summa cum laude*) and Ph.D. degrees in Electrical Engineering in 1981 and 1984, respectively, from the École polytechnique fédérale de Lausanne (EPFL), Switzerland. From 1985 to 1997, he worked as a scientist with the National Institutes of Health, Bethesda USA. He is now full professor and Director of the Biomedical Imaging Group at the EPFL. His main research area is biomedical image processing. He has a strong interest in sampling theories, multiresolution algorithms, wavelets, and the use of splines for image processing. He has published 200 journal papers on those topics, and is one of ISI's Highly Cited authors in Engineering (http://isihighlycited.com). Dr. Unser has held the position of associate Editor-in-Chief (2003-2005) for the IEEE Transactions on Medical Imaging and has served as Associate Editor for the same journal (1999-2002; 2006-2007), the IEEE Transactions on Image Processing (1992-1995), and the IEEE Signal Processing Letters (1994-1998). He is currently member of the editorial boards of Foundations and Trends in Signal Processing, and Sampling Theory in Signal and Image Processing. He co-organized the first IEEE International Symposium on Biomedical Imaging (ISBI2002) and was the founding chair of the technical committee of the IEEE-SP Society on Bio Imaging and Signal Processing (BISP). Dr. Unser received the 1995 and 2003 Best Paper Awards, the 2000 Magazine Award, and two IEEE Technical Achievement Awards (2008 SPS and 2010 EMBS). He is an EURASIP Fellow and a member of the Swiss Academy of Engineering Sciences.